

REPORT DOCUMENTATION PAGE				Form Approved OMB NO. 0704-0188	
<p>The public reporting burden for this collection of information is estimated to average 1 hour per response, including the time for reviewing instructions, searching existing data sources, gathering and maintaining the data needed, and completing and reviewing the collection of information. Send comments regarding this burden estimate or any other aspect of this collection of information, including suggestions for reducing this burden, to Washington Headquarters Services, Directorate for Information Operations and Reports, 1215 Jefferson Davis Highway, Suite 1204, Arlington VA, 22202-4302. Respondents should be aware that notwithstanding any other provision of law, no person shall be subject to any penalty for failing to comply with a collection of information if it does not display a currently valid OMB control number.</p> <p>PLEASE DO NOT RETURN YOUR FORM TO THE ABOVE ADDRESS.</p>					
1. REPORT DATE (DD-MM-YYYY)		2. REPORT TYPE New Reprint		3. DATES COVERED (From - To) -	
4. TITLE AND SUBTITLE Directed Self-Assembly of Epitaxial CoFeCoFe ₂ O ₄ -BiFeO ₃ Multiferroic Nanocomposites				5a. CONTRACT NUMBER W911NF-08-2-0032	
				5b. GRANT NUMBER	
				5c. PROGRAM ELEMENT NUMBER 611103	
6. AUTHORS Ryan Comes, Hongxue Liu, Mikhail Khokhlov, Richard Kasica, Jiwei Lu, Stuart A. Wolf				5d. PROJECT NUMBER	
				5e. TASK NUMBER	
				5f. WORK UNIT NUMBER	
7. PERFORMING ORGANIZATION NAMES AND ADDRESSES Cornell University Office of Sponsored Programs 373 Pine Tree Road Ithaca, NY 14850 -2820				8. PERFORMING ORGANIZATION REPORT NUMBER	
9. SPONSORING/MONITORING AGENCY NAME(S) AND ADDRESS(ES) U.S. Army Research Office P.O. Box 12211 Research Triangle Park, NC 27709-2211				10. SPONSOR/MONITOR'S ACRONYM(S) ARO	
				11. SPONSOR/MONITOR'S REPORT NUMBER(S) 54227-MS-MUR.42	
12. DISTRIBUTION AVAILABILITY STATEMENT Approved for public release; distribution is unlimited.					
13. SUPPLEMENTARY NOTES The views, opinions and/or findings contained in this report are those of the author(s) and should not be construed as an official Department of the Army position, policy or decision, unless so designated by other documentation.					
14. ABSTRACT CoFe ₂ O ₄ (CFO)/BiFeO ₃ (BFO) nanocomposites are an intriguing option for future memory and logic technologies due to the magnetoelectric properties of the system. However, these nanocomposites form with CFO pillars randomly located within a BFO matrix, making implementation in devices difficult. To					
15. SUBJECT TERMS multiferroic					
16. SECURITY CLASSIFICATION OF:			17. LIMITATION OF ABSTRACT UU	15. NUMBER OF PAGES	19a. NAME OF RESPONSIBLE PERSON Daniel Ralph
a. REPORT UU	b. ABSTRACT UU	c. THIS PAGE UU			19b. TELEPHONE NUMBER 607-255-9644

Report Title

Directed Self-Assembly of Epitaxial CoFe

ABSTRACT

CoFe₂O₄ (CFO)/BiFeO₃ (BFO) nanocomposites are an intriguing option for future memory and logic technologies due to the magnetoelectric properties of the system. However, these nanocomposites form with CFO pillars randomly located within a BFO matrix, making implementation in devices difficult. To overcome this, we present a technique to produce patterned nanocomposites through self-assembly. CFO islands are patterned on Nb-doped SrTiO₃ to direct the self-assembly of epitaxial CFO/BFO nanocomposites, producing square arrays of CFO pillars.

REPORT DOCUMENTATION PAGE (SF298)
(Continuation Sheet)

Continuation for Block 13

ARO Report Number 54227.42-MS-MUR

Directed Self-Assembly of Epitaxial CoFe ...

Block 13: Supplementary Note

© 2012 . Published in Nano Letters, Vol. 12 (5) (2012), (2 (5). DoD Components reserve a royalty-free, nonexclusive and irrevocable right to reproduce, publish, or otherwise use the work for Federal purposes, and to authorize others to do so (DODGARS §32.36). The views, opinions and/or findings contained in this report are those of the author(s) and should not be construed as an official Department of the Army position, policy or decision, unless so designated by other documentation.

Approved for public release; distribution is unlimited.

Directed Self-Assembly of Epitaxial CoFe_2O_4 – BiFeO_3 Multiferroic Nanocomposites

Ryan Comes,^{*,†} Hongxue Liu,[†] Mikhail Khokhlov,^{†,§} Richard Kasica,^{||} Jiwei Lu,[†] and Stuart A. Wolf^{†,‡}

[†]Department of Materials Science and Engineering and [‡]Department of Physics, University of Virginia, Charlottesville, Virginia 22904, United States

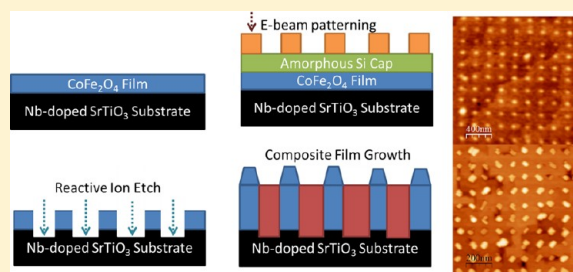
[§]Guilford College, Greensboro, North Carolina 27410, United States

^{||}Center for Nanoscale Science and Technology, National Institute of Standards and Technology, Gaithersburg, Maryland 20899, United States

S Supporting Information

ABSTRACT: CoFe_2O_4 (CFO)– BiFeO_3 (BFO) nanocomposites are an intriguing option for future memory and logic technologies due to the magnetoelectric properties of the system. However, these nanocomposites form with CFO pillars randomly located within a BFO matrix, making implementation in devices difficult. To overcome this, we present a technique to produce patterned nanocomposites through self-assembly. CFO islands are patterned on Nb-doped SrTiO_3 to direct the self-assembly of epitaxial CFO–BFO nanocomposites, producing square arrays of CFO pillars.

KEYWORDS: Directed self-assembly, multiferroics, nanocomposites, e-beam lithography, BiFeO_3 , CoFe_2O_4



Multiferroic nanocomposite films have been heavily studied for their potential applications in magnetoelectric systems.¹ The CoFe_2O_4 – BiFeO_3 (CFO and BFO, respectively) system has generated particular interest due to the magnetoelastic properties of CFO² and the combination of ferroelectricity and antiferromagnetism in BFO.³ It has been shown that when CFO and BFO are codeposited via physical vapor deposition at high temperatures on a SrTiO_3 (001) substrate that the materials will spontaneously phase segregate to produce an epitaxial CFO pillar in an epitaxial BFO matrix, which is referred to as a 1-3 nanocomposite.⁴ The CFO pillars form faceted structures with {110}-type interfaces with the BFO matrix and {111}-facets on the surface, protruding above the matrix.⁵ The pattern of the CFO pillars in the structure is essentially random, since they are formed through the nucleation of a CFO island on the substrate, while BFO wets the remaining surface. Thus, to control the location of the pillars, a means of controlling the nucleation site for the CFO island is needed. CFO–BFO composites have been found to demonstrate magnetoelectric coupling, allowing for electrical control of the magnetic anisotropy of the CFO pillars.^{6,7} Based on these properties, the composite system has been proposed for both magnetoelectric memory⁸ and logic⁹ applications. In particular, the reconfigurable array of magnetic automata (RAMA)^{9,10} is a nanomagnetic logic system based on the magnetic quantum cellular automata (MQCA) logic architecture¹¹ which would use a CFO–BFO 1-3 composite with the pillars arranged in a square array to create a reprogrammable logic system. However, in order to make devices using these

composites, the ability to place the pillars into predetermined arrays is required.

Previous work in patterning multiferroic nanocomposites has been limited. One method to produce patterned magnetoelectric composites is to use a porous anodic aluminum oxide (AAO) film as a liftoff mask during deposition, which produces a hexagonal array pattern.^{12,13} In one approach, a BTO–CFO multilayer is deposited onto the AAO film on a STO substrate, which yields a small amount of magnetoelectric response.¹² Another technique is to use the AAO film to form CFO islands and then overcoat the islands with ferroelectric $\text{Pb}(\text{Zr,Ti})\text{O}_3$ (PZT), which yields a composite that is both ferroelectric and ferromagnetic.¹³ Others have used a SiN membrane as a shadow mask to grow ferromagnetic $\text{La}_{0.7}\text{Sr}_{0.3}\text{MnO}_3$ islands and overcoat them with ferroelectric PbTiO_3 , which produces an epitaxial composite structure with submicrometer dots and intriguing ferroelectric domain structures.¹⁴ However, none of these techniques offers the degree of magnetoelectric control found in the BFO–CFO 1-3 epitaxial nanocomposites.^{6,8} Additionally, the AAO and membrane masks are not practical for the formation of a square array of pillars needed for the proposed memory and logic architectures. Another approach involves the use of block copolymers to order the formation of polycrystalline CFO pillars in a polycrystalline PZT matrix using a sol–gel process.¹⁵ This technique also produces a hexagonal array of pillars but demonstrates a stronger

Received: January 26, 2012

Revised: April 5, 2012

Published: April 9, 2012

magnetoelectric response than found in the other works. Larger, micrometer-scale polycrystalline CFO islands embedded in a PbTiO_3 matrix have been fabricated using e-beam lithography (EBL) via a liftoff process, but such techniques are more difficult for smaller nanoscale islands and may not produce the epitaxial pillars and matrix that are desired.¹⁶ A bottom-up technique to arbitrarily define the location of individual pillars in the composite would be ideal for future technologies.

Templated self-assembly is a popular technique to control the formation of a self-assembled structure.^{17,18} In this approach, the surface of a substrate is modified to constrain how a pattern will form during thin film deposition. Focused ion beam (FIB) patterning of a Si substrate to form pits has been shown to be effective in creating a preferred nucleation site for the formation of Ge epitaxial quantum dots.^{19,20} Similarly, EBL has been used to form SiC on the substrate surface, which acts as a nucleation site during Ge quantum dot growth.²¹ However, no reports of templating the growth of oxide composites have been found. In this work, we demonstrate the growth of self-assembled BFO–CFO 1-3 nanocomposites with the pillars patterned into a square array through the use of a substrate with CFO islands on the surface patterned using EBL.

A top-down lithographic process is employed to pattern CFO islands on the substrate surface, followed by a bottom-up self-assembly process to produce the ordered CFO–BFO nanocomposite. A full schematic of the fabrication process is shown in Figure 1. A 0.5% Nb-doped STO (Nb:STO) (001) conductive substrate was prepared using common etching and annealing techniques to produce a TiO_2 terminated surface with step edges due to substrate miscut.²² A 12 nm CFO film

was then deposited on the substrate using pulsed electron deposition (PED).^{23,24} The CFO film grows via the Volmer–Weber epitaxial growth mode, producing epitaxial islands on the surface.²⁵ An atomic force microscopy (AFM) surface topography scan after the growth is shown in Figure 2a. The sample was found to have islands uniformly coating the surface with diameters between 25 and 50 nm.

An amorphous 20 nm Si capping layer was then sputtered onto the surface of the CFO film in a cleanroom environment. The Si capping layer has previously been shown to be useful in promoting adhesion of hydrosilanesquioxane (HSQ) negative-tone e-beam resist and also acts as a sacrificial etch mask later in the process.²⁶ HSQ resist was spin coated onto the Si capping layer, and arrays of dots 50 nm in diameter with center-to-center distances (pitch) of 100, 150, and 200 nm were then written onto a single substrate, which can be seen in Figure 2b. A scanning electron microscope (SEM) image of the patterned array with 200 nm center-to-center spacing (pitch) is shown in Figure 2c. The pattern was then transferred into the Si capping layer using a reactive ion etch (RIE) with a mixture of SF_6 and O_2 gases. Finally, the remaining pattern of HSQ and Si pillars was used as a sacrificial mask for an Ar ion etch using the RIE system. An AFM scan of the islands following the etching step is shown in Figure 2d, along with cross-sectional height data in Figure 2e. The CFO islands are between 3 and 4 nm tall. It is interesting to note that following the etching process, step edges from the original substrate annealing process are again visible, indicating a high-quality STO surface for the growth of the composite film.

The patterned substrate was then used as a template for a second film grown using the PED system. Details of the deposition conditions are available in the Supporting Information. An initial 1 nm BFO film was grown by ablating only the BFO target with 20 at. % excess bismuth, which wets the surface and prevents formation of CFO pillars away from the patterned region. BFO is believed to preferentially grow on the substrate surface and leave the CFO pillars relatively unaffected due to the lattice mismatch and immiscibility of the perovskite and spinel phases. Immediately after the conclusion of the initial BFO deposition, the CFO gun was activated, and a codeposition was performed, producing an overall BFO thickness of approximately 25 nm based on X-ray reflectivity measurements.

The resulting film was characterized using an Asylum Research Cypher AFM system. AFM analysis was performed on the arrays with pillar pitches of 100, 150, and 200 nm. Images for all three dimensions are shown in Figure 3, along with cross-sectional height data for each image. The 100 and 150 nm pitch arrays have uniformly distributed pillars with no interstitial pillars present. In the 200 nm arrays, some small CFO pillars nucleated in spite of the initial BFO wetting layer, an example of which is highlighted with a diamond in Figure 3c. A key issue is whether the codeposited CFO preferentially and completely segregates to the pillar sites. To address this, detailed statistical analysis of the AFM measurements for each of the three pitch sizes is shown in Table 1. The average pillar height and width above the surface are shown for each of the pitch sizes, which allows for the calculation of the volume of CFO phase held above the surface of the BFO matrix at the template sites for each array. The calculated volume per unit area for all three pitch sizes is shown in Table 1, with the values normalized such that the value for the 100 nm array is equal to 1. Based on this data, we are able to show that the 100 and 150

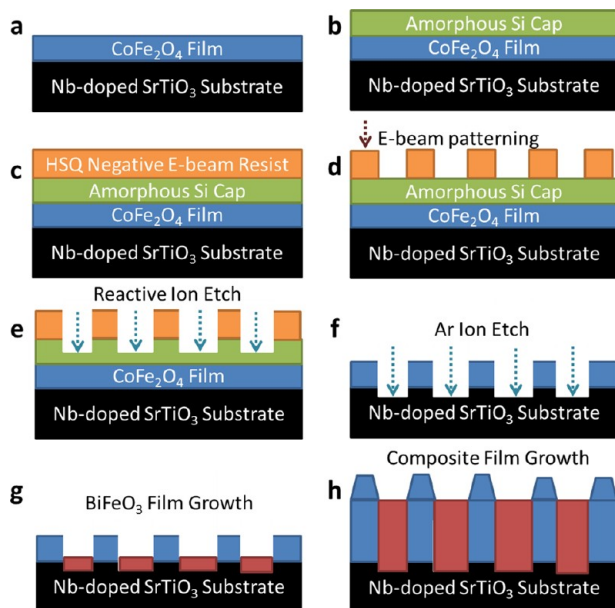


Figure 1. Flowchart for the fabrication process. (a) Deposition of CoFe_2O_4 (CFO) film using PED. (b) Deposition of amorphous Si capping layer using RF sputtering. (c) Spin coating of sample with HSQ negative-tone e-beam resist. (d) Patterning of pillars using EBL. (e) Reactive ion etching of Si cap. (f) Ar ion etching of CFO film. (g) Deposition of 1 nm thick BiFeO_3 (BFO) film using PED. (h) Codeposition of CFO and BFO using PED to form an epitaxial nanocomposite.

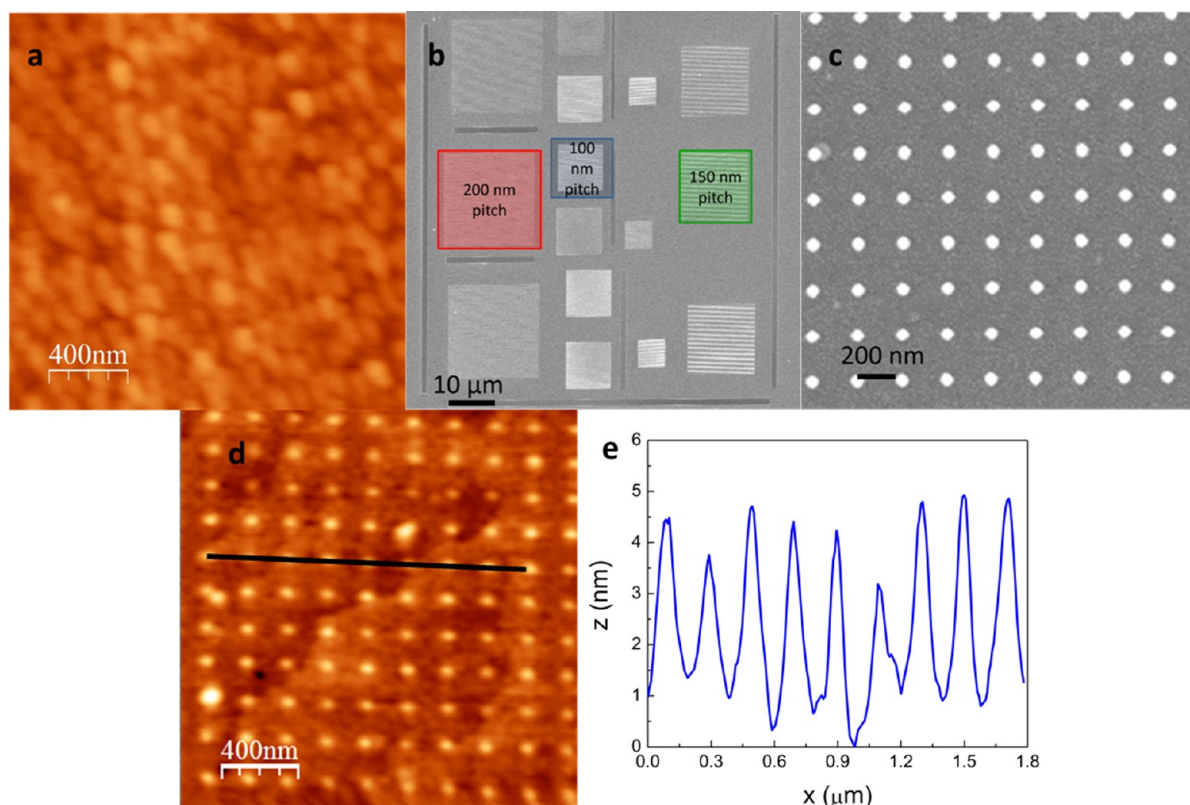


Figure 2. (a) AFM image of uniform CFO film used for template pattern showing regular epitaxial islands on the surface. (b) SEM image showing the configuration of arrays on a single sample after EBL. (c) SEM image of EBL-patterned 200 nm pitch array before etching. (d) AFM image of CFO islands after RIE step, showing uniform 200 nm spacing and substrate step edges which are preserved. (e) AFM cross section along black line in (d).

nm arrays have similar CFO volume per unit area (1 and 1.02, respectively) above the surface. This means that CFO mass is conserved above the surface of the matrix. The pillar area coverage for the 100 and 150 nm arrays is also similar. Since the pillars are not expected to deviate substantially in diameter during the film growth, this is an indication that the volume of CFO below the surface of the BFO matrix is equal as well. This result agrees with the work of Zheng, et al., (ref 4), which showed that the area coverage of the pillars beneath the matrix surface is equal to the volume fraction of CFO in the adatom flux.⁴ Thus, all CFO flux deposited in the 100 and 150 nm pitch arrays segregates to the pillars at the template sites.

For the 200 nm pitch array, there is excess CFO volume above the surface, as shown by the 1.10 normalized volume per unit area in Table 1. A close inspection of Figure 3c shows that the pillars are more irregularly shaped than in the two arrays with smaller pitch, which indicates that the pillars are most likely not forming the ideal faceted interface with the BFO matrix that is seen in the other arrays. The fractional area coverage of the pillars at the template sites in array is also substantially reduced, meaning that the pillar volume is not sufficient to account for the amount of CFO deposited in the region. The interstitial CFO pillars which form within the BFO matrix in the 200 nm pitch array account for the remainder of the CFO mass within the array.

An analysis of the surface diffusion length for the CFO adatoms is useful to elucidate the kinetics of the growth process. It is clear from the AFM analysis of both the 100 and 150 nm pitch arrays that all CFO flux is captured at the template sites. However, this is not the case in the 200 nm pitch

array. It would appear that the diffusion length of the CFO adatoms is not sufficient for flux that lands far from any of the template sites to move to one of the sites. The maximum diffusion length, L , required for adatoms landing in the BFO matrix to reach a template site is given by

$$L = \frac{\sqrt{2}}{2}P - r \quad (1)$$

where P is the array pitch and r is the radius of the pillar. This maximum distance occurs for adatoms that land equidistant from all four neighboring template sites at the center of the square formed by the sites. For the 150 nm pitch with a pillar radius of 27 nm, L is equal to approximately 79 nm, and for the 200 nm pitch with a 30 nm diameter, L is equal to 111 nm. Thus we would expect the diffusion length to fall between 79 and 111 nm. The surface diffusion length, d , of CFO adatoms can be determined using the formula:

$$d = \sqrt{4Dt} \quad (2)$$

where D is the surface diffusivity and t is the deposition time to form a unit cell monolayer of BFO in the matrix, which is inversely proportional to the deposition rate. The diffusivity, D , is a temperature-dependent parameter given by

$$D = D_0 e^{-E_a/kT} \quad (3)$$

where k is Boltzmann's constant, T is the surface temperature of the sample, E_a is the activation energy for surface diffusion and D_0 is a constant which depends in part on the diffusion geometry but is nominally independent of temperature. Zheng et al. (ref 4) previously performed calculations to determine the

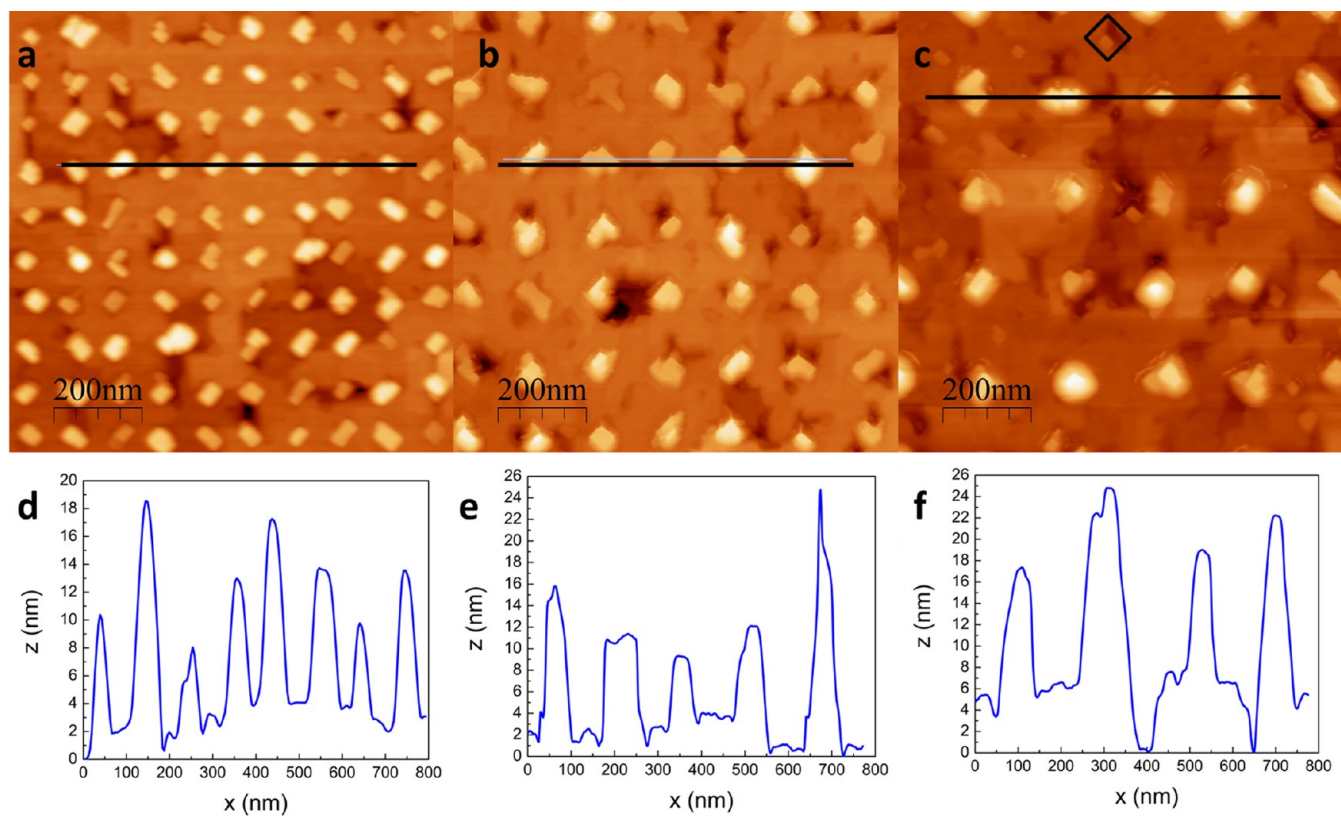


Figure 3. (a) Pillar topography with 100 nm center-to-center distance (pitch). (b) Pillar topography with 150 nm pitch. (c) Pillar topography with 200 nm pitch, with defect CFO pillar highlighted. (d–f) Cross section data for: (d) 100, (e) 150, and (f) 200 nm AFM images along the black lines shown in (a–c).

Table 1. Pillar Dimensions Measured via AFM in Figure 3

pillar spacing (nm)	mean pillar side length (nm)	mean pillar height above matrix surface (nm)	fractional area coverage (%)	CFO pillar volume above surface in constant area (normalized)
100	41	6.1	16	1.00
150	55	7.6	15	1.02
200	61	11.8	9	1.10

activation energy for surface diffusion, E_a , of CFO adatoms in the BFO matrix and found a value of 1.66 eV with no stated uncertainty. By further analyzing the results presented in that work, we can perform a linear fit to estimate the value for D_0 and find a value of $1.34 \pm 0.91 \times 10^{10} \text{ nm}^2/\text{sec}$.⁴ For further

details on the fitting calculation and assumptions involved, see the Supporting Information. With the value of D_0 determined and the published value of E_a with a small uncertainty of 0.05 eV assumed, it becomes possible to estimate the diffusion length of the CFO adatom flux. We find a value for $d = 55 \pm 26 \text{ nm}$, which is in reasonable agreement with the experimental results, since $L = 79 \text{ nm}$ is within the uncertainty of the calculation for d . This shows that interstitial pillars only form in the 200 nm pitch array due to the kinetic limitations during the growth. In order to produce a high-quality array with pillar spacing of 200 nm, a slower deposition rate or higher substrate temperature would be required, which could increase the adatom diffusion length.

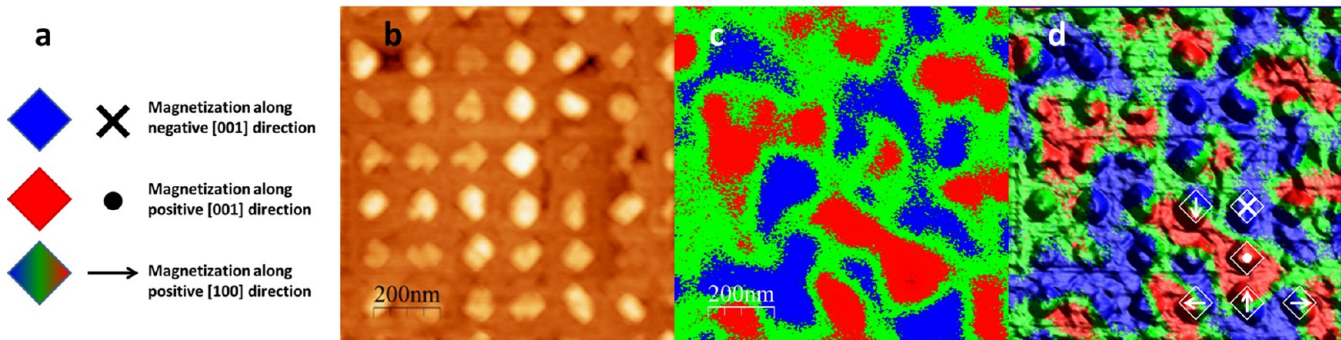


Figure 4. (a) Schematic of MFM phase contrasts for both in- and out-of-plane magnetizations. (b) Topography image of 150 nm pitch array from MFM measurement. (c) Out-of-plane MFM phase image of array. (d) Phase contrast overlaid on three-dimensional rendering of topography with examples of magnetization along each direction shown for certain pillars.

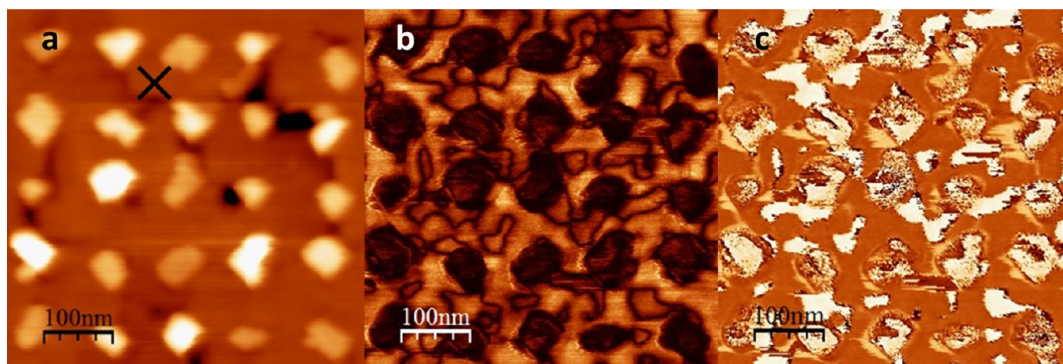


Figure 5. (a) Contact mode topography image taken during PFM measurement ('X' indicates the site of SS-PFM measurement in Figure 6). (b) Ferroelectric amplitude image corresponding to (a) (dark indicates low PFM response). (c) Ferroelectric phase image corresponding to (a) (white and orange correspond to oppositely oriented domains along the out-of-plane direction).

The results of the AFM and simple diffusion analysis above are a good demonstration of the nature of the templating in this work. We have shown that the CFO islands patterned on the substrate surface act as attachment sites for the epitaxial CFO pillars that form within the BFO matrix and that attachment only occurs at those sites unless there are kinetic limitations—primarily the surface diffusion length. Thus, arbitrary pitch sizes of as much as hundreds of nanometers may be possible by tailoring the growth conditions, such as the growth temperature and the deposition rate, to the template pattern. In addition, smaller pitch sizes should be readily achievable by refining the EBL and ion etching processes to improve resolution.

It is worthwhile to characterize the magnetic and ferroelectric properties of the composite as a means of comparing the template sample with other unpatterned composites in the literature. Conventional measurements to determine the magnetic anisotropy in the sample through the use of a vibrating sample magnetometer (VSM) or superconducting quantum interference device (SQUID) would be fruitless, however, as the patterned arrays cover only about 0.01% of the overall surface and any signal would be masked by the pillars that form spontaneously outside of the patterned arrays. Thus, magnetic force microscopy (MFM) is the only viable approach to study the anisotropy characteristics of the pillars.

The sample was demagnetized by an applied in-plane damped oscillatory magnetic field in order to drive the pillars to the minimum energy magnetization state. Figure 4 shows MFM scans of the 150 nm pitch array after the demagnetization process, with a three-dimensional rendering of the topography shown and the magnetic phase overlaid as the color in the image. In Figure 4b,c, red and blue represent the positive and negative out-of-plane magnetizations (arbitrary sign), while green represents regions of small magnetic response. The nature of the magnetostatic interactions between neighboring pillars with in-plane magnetization makes the interpretation of the MFM images complicated. If the pillars are magnetized in-plane, the MFM phase contrast should be positive on one side of the pillar and negative on the other, with a neutral region in the center of the pillar due to the nature of the magnetic dipole fringe field that curls over the surface. For pillars with out of plane magnetization, the phase should be uniform across the surface of the pillar. A schematic of the two configurations is shown in Figure 4a.

Figure 4d shows the MFM phase contrast overlaid on a three-dimensional rendering of the surface topography. This technique is useful to show which pillars have in- and out-of-

plane magnetization. Examples of magnetization along all six possible directions are highlighted in the figure. There is no clear preference for in- or out-of-plane magnetization, indicating that uniaxial anisotropy in the pillars is minimal and that the magnetocrystalline anisotropy in CFO along the three [100] axes dominates the magnetic behavior. This result, while different from many reports in the literature, agrees with other composite films grown by PED in our group.²⁷ We have previously shown²⁷ that the relatively slow growth rate ($\sim 1\text{--}3$ Å/min) achieved using the PED technique allows for full relaxation of residual out-of-plane compressive strain in the pillars, which is the origin of the perpendicular anisotropy seen in other CFO–BFO nanocomposites.^{28,29}

To characterize the ferroelectric properties of the sample, piezoresponse force microscopy (PFM) was performed. PFM results topography, amplitude, and phase scans are shown in Figure 5. The amplitude scan (Figure 5b) shows that there is no ferroelectric response from the CFO pillars, indicated by the black coloring at pillar sites. The amplitude scan also shows that there is a high density of 180° domain walls in the BFO matrix, as indicated by the dark lines throughout the pattern where the ferroelectric response vanishes.³⁰ The phase image shows clear domains which are 180° out-of-phase, in agreement with the amplitude scan. The domain structure of the composite is consistent with results shown elsewhere, with small 180° reverse domains forming near the interface with the pillars.³¹

Localized ferroelectric hysteresis measurements were also performed using switching spectroscopy PFM (SS-PFM) within the matrix region shown in Figure 5.³² The location of the measurement is marked with an 'X' in Figure 5a. Additional measurements were made at other sites in the BFO matrix within the 500 nm scan area and showed similar results. Further details of this technique and the data analysis can be found in the Supporting Information. The hysteresis loops are shown in Figure 6. Figure 6a shows the out-of-plane phase, with clear switching at applied voltages of approximately 2.5 V. The measured tip displacement amplitude is shown in Figure 6b, with the traditional butterfly curve shape. Estimates of the value of the piezoelectric d_{33} coefficient are difficult due to the complex nature of the tip–sample interactions, but estimations can be made using the measured tip displacement shown in Figure 6b.³³ For details on this analysis, see the Supporting Information. The estimated value for d_{33} is 5–10 pm/V, which is significantly lower than the 40–80 pm/V seen elsewhere in the literature for uniform BFO films.³⁴ However, this result is expected and has been seen in other SS-PFM measurements of

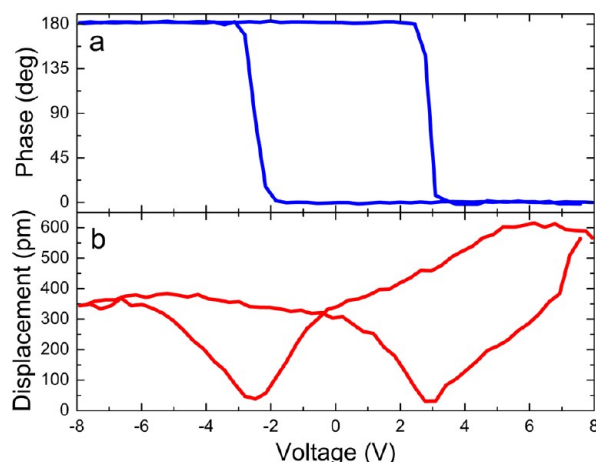


Figure 6. (a) Out-of-plane ferroelectric phase loop in BiFeO₃ (BFO) matrix measured using PFM. (b) Measured tip displacement showing the expected butterfly loop behavior.

nanocomposites due to the highly localized electric field originating from the small PFM tip.³⁵ Measurements made with electrode contacts would be expected to show somewhat larger values for d_{33} .

In conclusion, we have demonstrated a new technique for the growth of ordered epitaxial CoFe₂O₄–BiFeO₃ nanocomposites using a top-down patterning process followed by a bottom-up template film growth. This technique is more flexible than the techniques used to create other ordered nanocomposites in that arbitrary patterns can be formed through the EBL process. The technique also allows for the formation of the epitaxial 1-3 nanocomposites that have been shown to have large magneto-electric response. Arrays of CFO nanopillars with pitches of 100, 150, and 200 nm have been fabricated, and their structural properties have been characterized. It is shown that for both the 100 and 150 nm pitches, all CFO deposited within the patterned regions are absorbed by the template pillars, with no interstitial defect pillars forming. The magnetic properties of the CFO pillars have been characterized via MFM, and the pillars have been shown to have minimal uniaxial anisotropy, which is in agreement with nanocomposite films grown without templating via PED. The PFM measurements demonstrated clean ferroelectric response in the BFO matrix, the hysteresis loops were measured, and the d_{33} out-of-plane piezoelectric response has been calculated.

■ ASSOCIATED CONTENT

Supporting Information

Detailed growth and fabrication techniques for the initial CoFe₂O₄ film, amorphous Si capping layer, HSQ resist, EBL patterning and development, reactive ion etching, and CoFe₂O₄–BiFeO₃ nanocomposite. Detailed explanations for the diffusion length calculations are also available along with the assumptions used. A discussion of the analysis of the PFM images and hysteresis loops is also included, detailing the calculations of the value of the piezoelectric d_{33} value. This material is available free of charge via the Internet at <http://pubs.acs.org>.

■ AUTHOR INFORMATION

Corresponding Author

*E-mail: rcomes@virginia.edu.

Notes

The authors declare no competing financial interest.

■ ACKNOWLEDGMENTS

The authors gratefully acknowledge funding from the Nano-electronics Research Initiative, NSF (DMR-08-19762) and DARPA (HR-0011-10-1-0072). R.C. also wishes to acknowledge funding from the National Defense Science and Engineering Graduate Fellowship. Research performed in part at the National Institute of Standards and Technology (NIST) Center for Nanoscale Science and Technology. The authors would also like to thank Prof. Jerrold Floro for helpful comments on the work.

■ REFERENCES

- (1) Yan, L.; Yang, Y.; Wang, Z.; Xing, Z.; Li, J.; Viehland, D. *J. Mater. Sci.* **2009**, *44*, 5080–5094.
- (2) Bozorth, R. M.; Tilden, E. F.; Williams, A. J. *Phys. Rev.* **1955**, *99*, 1788.
- (3) Kubel, F.; Schmid, H. *Acta Crystallogr., Sect. B: Struct. Sci.* **1990**, *46*, 698–702.
- (4) Zheng, H.; Straub, F.; Zhan, Q.; Yang, P.-L.; Hsieh, W.-K.; Zavaliche, F.; Chu, Y.-H.; Dahmen, U.; Ramesh, R. *Adv. Mater.* **2006**, *18*, 2747–2752.
- (5) Zheng, H.; Zhan, Q.; Zavaliche, F.; Sherburne, M.; Straub, F.; Cruz, M. P.; Chen, L.-Q.; Dahmen, U.; Ramesh, R. *Nano Lett.* **2006**, *6*, 1401–1407.
- (6) Zavaliche, F.; Zheng, H.; Mohaddes-Ardabili, L.; Yang, S. Y.; Zhan, Q.; Shafer, P.; Reilly, E.; Chopdekar, R.; Jia, Y.; Wright, P.; Schlom, D. G.; Suzuki, Y.; Ramesh, R. *Nano Lett.* **2005**, *5*, 1793–1796.
- (7) Yan, L.; Wang, Z.; Xing, Z.; Li, J.; Viehland, D. *J. Appl. Phys.* **2010**, *107*, 064106.
- (8) Zavaliche, F.; Zhao, T.; Zheng, H.; Straub, F.; Cruz, M. P.; Yang, P.-L.; Hao, D.; Ramesh, R. *Nano Lett.* **2007**, *7*, 1586–1590.
- (9) Wolf, S. A.; Lu, Jiwei; Stan, M. R.; Chen, E.; Treger, D. M. *Proc. IEEE* **2010**, *98*, 2155–2168.
- (10) Kabir, M.; Stan, M. R.; Wolf, S. A.; Comes, R. B.; Lu, J. In *Proceedings of the Great Lakes Symposium on VLSI, GLSVLSI 2011*, Lausanne, Switzerland, May 2–4, 2011; ACM: New York, 2011; pp 25–30.
- (11) Cowburn, R. P.; Welland, M. E. *Science* **2000**, *287*, 1466–1468.
- (12) Lu, X.; Kim, Y.; Goetze, S.; Li, X.; Dong, S.; Werner, P.; Alexe, M.; Hesse, D. *Nano Lett.* **2011**, *11*, 3202–3206.
- (13) Gao, X.; Rodriguez, B. J.; Liu, L.; Birajdar, B.; Pantel, D.; Ziese, M.; Alexe, M.; Hesse, D. *ACS Nano* **2011**, *4*, 1099–1107.
- (14) Vrejoiu, I.; Morelli, A.; Johann, F.; Biggemann, D. *Appl. Phys. Lett.* **2011**, *99*, 082906.
- (15) Ren, S.; Briber, R. M.; Wuttig, M. *Appl. Phys. Lett.* **2008**, *93*, 173507.
- (16) Ding, L.-Y.; Wu, F.-X.; Chen, Y.-B.; Gu, Z.-B.; Zhang, S.-T. *Appl. Surf. Sci.* **2011**, *257*, 3840–3842.
- (17) Whitesides, G. M.; Grzybowski, B. *Science* **2002**, *295*, 2418–2421.
- (18) Cheng, J. Y.; Ross, C. A.; Smith, H. I.; Thomas, E. L. *Adv. Mater.* **2006**, *18*, 2505–2521.
- (19) Gherasimova, M.; Hull, R.; Reuter, M. C.; Ross, F. M. *Appl. Phys. Lett.* **2008**, *93*, 023106.
- (20) Graham, J. F.; Kell, C. D.; Floro, J. A.; Hull, R. *Nanotechnology* **2011**, *22*, 075301.
- (21) Guise, O.; Yates, J. T.; Levy, J.; Ahner, J.; Vaithyanathan, V.; Schlom, D. G. *Appl. Phys. Lett.* **2005**, *87*, 171902.
- (22) Kawasaki, M.; Takahashi, K.; Maeda, T.; Tsuchiya, R.; Shinohara, M.; Ishiyama, O.; Yonezawa, T.; Yoshimoto, M.; Koinuma, H. *Science* **1994**, *266*, 1540–1542.
- (23) Strikovski, M.; Harshavardhan, K. S. *Appl. Phys. Lett.* **2003**, *82*, 853–855.

- (24) Comes, R.; Gu, M.; Khokhlov, M.; Lu, J.; Wolf, S. A. *J. Magn. Mater.* **2012**, *324*, 524–527.
- (25) Huang, W.; Zhou, L. X.; Zeng, H. Z.; Wei, X. H.; Zhu, J.; Zhang, Y.; Li, Y. R. *J. Cryst. Growth* **2007**, *300*, 426–430.
- (26) Wi, J.-S.; Lee, T.-Y.; Jin, K.-B.; Hong, D. H.; Shin, K. H.; Kim, K.-B. *J. Vac. Sci. Technol., B* **2006**, *24*, 2616–2620.
- (27) Comes, R.; Khokhlov, M.; Liu, H.; Lu, J.; Wolf, S. A. *J. Appl. Phys.* **2012**, *111*, 07D914–07D914–3.
- (28) Dix, N.; Muralidharan, R.; Guyonnet, J.; Warot-Fonrose, B.; Varela, M.; Paruch, P.; Sanchez, F.; Fontcuberta, J. *Appl. Phys. Lett.* **2009**, *95*, 062907–062907–3.
- (29) Oh, Y. S.; Crane, S.; Zheng, H.; Chu, Y. H.; Ramesh, R.; Kim, K. H. *Appl. Phys. Lett.* **2010**, *97*, 052902.
- (30) Rodriguez, B. J.; Callahan, C.; Kalinin, S. V.; Proksch, R. *Nanotechnology* **2007**, *18*, 475504.
- (31) Rodriguez, B. J.; Jesse, S.; Baddorf, A. P.; Zhao, T.; Chu, Y. H.; Ramesh, R.; Eliseev, E. A.; Morozovska, A. N.; Kalinin, S. V. *Nanotechnology* **2007**, *18*, 405701.
- (32) Jesse, S.; Baddorf, A. P.; Kalinin, S. V. *Appl. Phys. Lett.* **2006**, *88*, 062908.
- (33) Proksch, R.; Kalinin, S. *Piezoresponse Force Microscopy with Asylum Research AFMs*.
- (34) Wang, J.; Neaton, J. B.; Zheng, H.; Nagarajan, V.; Ogale, S. B.; Liu, B.; Viehland, D.; Vaithyanathan, V.; Schlom, D. G.; Waghmare, U. V.; Spaldin, N. A.; Rabe, K. M.; Wuttig, M.; Ramesh, R. *Science* **2003**, *299*, 1719–1722.
- (35) Tan, Z.; Roytburd, A. L.; Levin, I.; Seal, K.; Rodriguez, B. J.; Jesse, S.; Kalinin, S.; Baddorf, A. *Appl. Phys. Lett.* **2008**, *93*, 074101.